Chemically Controllable Magnetic Transition Temperature and Magneto-Elastic Coupling in MnZnSb Compounds

Philip A. E. Murgatroyd, Kieran Routledge, Samantha Durdy, Michael W. Gaultois, T. Wesley Surta, Matthew S. Dyer, John B. Claridge, Stanislav N. Savvin, Denis Pelloquin, Sylvie Hébert, and Jonathan Alaria*

Magneto-caloric materials offer the possibility to design environmentally friendlier thermal management devices compared to the widely used gas-based systems. The challenges to develop this solid-state based technology lie in the difficulty of finding materials presenting a large magneto-caloric effect over a broad temperature span together with suitable secondary application parameters such as low heat capacity and high thermal conductivity. A series of compounds derived from the PbFCl structure is investigated using a combination of computational and experimental methods focusing on the change of cell volume in magnetic and non-magnetic ground states. Scaling analysis of the magnetic properties determines that they are second order phase transition ferromagnets and that the magnetic entropy change is driven by the coupling of magneto-elastic strain in the square-net through the magnetic transition determined from neutron and synchrotron X-ray diffraction. The primary and secondary application related properties are measured experimentally, and the c/a parameter is identified as an accurate proxy to control the magnetic transition. Chemical substitution on the square-net affords tuning of the Curie temperature over a broad temperature span between 252 and 322 K. A predictive machine learning model for the c/a parameter is developed to guide future exploratory synthesis.

1. Introduction

Near room-temperature magnetic refrigeration based on the magneto-caloric effect (MCE) is a potentially efficient and environmentally friendly technology[1,2] with the potential to replace conventional gas-compression cooling systems which are estimated to be responsible for ≈8% of global CO_2 emissions. It takes advantage of the excess entropy present in a magnetically ordered material and the possibility of heat extraction through thermodynamic cycles, equivalent to the conventional vapor-compression cycle where alternating adiabatic and isothermal magnetizations and demagnetizations are performed. This effect has achieved extremely low temperatures using paramagnetic salts,[3] however the deployment of domestic cooling devices has so far been challenging. In a ferromagnetic compound, the MCE is largest around the Curie temperature (T_C) where magnetic fluctuations are maximal, thus limiting the number of candidate materials to compounds presenting a $T_C \approx 250–290$ K. A simple consideration of the upper theoretical limit of the molar magnetic entropy given by $S_{mag} = R\ln(2J + 1)$, where R is the universal gas constant and J is the total angular momentum, makes elemental Gd ($J = 7/2$) the prototypical magnetocaloric material for domestic applications due to its large saturation magnetization, T_C of 292 K, and sizeable isothermal entropy change $\Delta S_{M(2T)} \approx 5.75$ J kg^{-1} K^{-1}.[4] Another mechanism driving a giant MCE ($\Delta S_{M(2T)} \approx 20$ J kg^{-1} K^{-1}) in magnetic materials,

P. A. E. Murgatroyd, K. Routledge, Dr. J. Alaria
Department of Physics
University of Liverpool
Oxford Street, Liverpool L69 7ZE, UK
E-mail: jonathan.alaria@liverpool.ac.uk

S. Durdy, Dr. M. W. Gaultois
Leverhulme Research Centre for Functional Materials Design
The Materials Innovation Factory
University of Liverpool
51 Oxford Street, Liverpool L7 3NY, UK

S. Durdy
Department of Computer Science
University of Liverpool
Ashton Street, Liverpool L69 3BX, UK

Dr. M. W. Gaultois, Dr. T. W. Surta, Dr. M. S. Dyer, Dr. J. B. Claridge
Department of Chemistry
University of Liverpool
Crown Street, Liverpool L69 7ZD, UK

Dr. S. N. Savvin
Institut Laue–Langevin
71 Avenue des Martyrs, Grenoble 38000, France

Dr. D. Pelloquin, Dr. S. Hébert
CRISMAT UMR 6508, 6 Boulevard du Maréchal Juin – F-14050
Caen cedex 4, France

ADVANCED
SCIENCE NEWS

www.advancedsciencenews.com

ADVANCED
FUNCTIONAL
MATERIALS

www.afm-journal.de

first observed in Gd-alloys,[5] is the strong coupling between one or more magnetic transitions with a first order phase transition (FOPT) such as structural,[6,7] or magneto-elastic transitions.[8] While these materials present good primary application related properties, the origin of the giant MCE poses engineering challenges due to the large thermal and magnetic hysteresis associated with the FOPT. These issues lead to lower efficiencies and mechanical degradation when cycling through the structural transition. Recently, a detailed assessment of a wide range of magnetocaloric families highlighted the importance of assessing secondary performance metrics such as heat capacity, density, thermal conductivity, and criticality aspects when evaluating the applicability of the compounds.[9] The search for magnetocaloric materials has largely been focused upon FOPT compounds whereas second order phase transition (SOPT) materials, presenting better mechanical stability and smaller hysteresis, are limited to Gd and its alloys,[9] manganite perovskites,[10,11] and austenite Heusler alloys.[12]

The complexity in designing new magnetocaloric materials lies in the various competing interactions which need to be considered to fulfill the primary application related properties. Phenomenological models to describe the observed MCE, such as the Bean–Rodbell model[13] have been developed ad-hoc, but have limited predictive ability.[14] Advances in density functional theory combined with data mining and machine learning algorithms have led to the successful development of computational proxies that can be used to identify non-trivial functional properties such as thermoelectric,[15] photovoltaic,[16] and magnetocaloric materials.[17] It is worth noting that the most successful examples do not necessarily rely on large datasets or comprehensive computational studies but rather on limiting the models to low-cost property calculations and targeted material families exhibiting common features in their chemistry. In a view to accelerate the identification of new magnetocaloric materials, the magnetic deformation Σ_M computational proxy was developed and tested by Bocarsly et al.[17] to isolate compounds presenting strong magneto-structural coupling without the necessity to present a FOPT.[18] MnZnSb possesses a Curie temperature just above room temperature and its adiabatic temperature change $\Delta T_{ad} = 0.4$ K/T, measured by direct method has recently been reported.[19] The magnetic deformation of this compound and other ferromagnetic compounds belonging to this family were not calculated in the original work performed by Bocarsly et al.[17] Thus, we calculated Σ_M for three ferromagnetic compounds belonging to the anti-PbFCl family and found values of 1.88, 2.26 and 2.24% for MnZnSb ($T_C = 304$ K), MnGaGe ($T_C = 450$ K[20]) and MnAlGe ($T_C = 503$ K[21]) respectively. These values all exceed the 1.5% threshold outlined by Bocarsly et al. to identify potential magnetocaloric materials.[17] As MnGaGe and MnAlGe have transition temperatures far from room temperature, they were not considered further. These preliminary results and previous reports motivated a detailed magneto-caloric investigation of MnZnSb to further our understanding of the magnetic phase transition with a view to tailor the MCE effect in these materials.

2. Results and Discussion

MnZnSb is closely related to Mn_2Sb which crystallizes in the tetragonal space group $P4/nmm$ with an anti-PbFCl structure described by Mn(I) sites arranged in series of 2D square nets with Mn(II) and Sb sites between, or as an NaCl-like structure, where the atom types alternate in all directions[22] as shown in **Figure 1**a. Ge-doped Mn_2Sb has shown a large magnetocaloric effect at the field induced first-order ferri-antiferromagnetic transition[23] and the substitution of the Mn(II) sites by Zn cations have been reported to result in no apparent structural changes[22] and the stabilization of a pseudo 2D itinerant ferromagnetic ground state with a reduced transition temperature ($T_C = 305$ K).[24] The spin-polarized density of states (DOS) and electronic band structure, with atomic and orbital projection, calculated for MnZnSb using PBE-GGA (Perdew–Burke–Ernzerhor-generalized gradient approximation) in a collinear ferromagnetic configuration, are shown in Figure 1b,c respectively. The delocalized, itinerant character of the Mn 3d-electron is evident from the partial DOS and is similar to that of the 3d states of the Mn(I) sites in Mn_2Sb which forms a broad energy-band.[25] The electronic band structure presents some s-p character at the Fermi level from Sb hybridization as seen in Figure 1c. MnZnSb powder was synthesized and appeared to be single phase from powder X-ray diffraction measurements with diffraction peaks assigned to the tetragonal PbFCl structure of MnZnSb phase with micron sized crystallites presenting the correct stoichiometry (Figure S1, Supporting Information). The calculated magnetic moment using experimental lattice parameters was 2.76 μ_B/f.u. and is significantly higher than the experimentally measured value of 1.6(2) μ_B/f.u. obtained from the saturation magnetization measured at 2 K (Figure S2, Supporting Information). This experimental moment is lower than what would be expected for a localized Mn atom based on typical oxidation states and further highlights the itinerant character of this system, this also supports the assignment of the unusual Mn^{1+} state upon the Mn(I) site by Johnson and Jeitschko.[22] This discrepancy between experiment and theory highlights that the hybridization, and delocalization, of the Mn d states is underestimated in first principles calculations at the PBE-GGA level. As can be seen in Table S1, Supporting Information, the accuracy of the theoretical magnetic moment for MnAlGe and MnGaGe improves when the PBEsol functional is used compared to standard PBE-GGA, however this improvement was not as significant for MnZnSb. This deviation between the DFT and experimental moment may suggest some local disorder or deviation from stoichiometry on the Mn(I) site in the MnZnSb.[22,26] As can be seen in Table S1, Supporting Information, DFT calculations based on relaxed structures with local disorder or deviation from stoichiometry, with an anti-ferromagnetic contribution, led to a decrease in moment that approaches the experimental value. It is important to note that the proxy of Bocarsly et al. was designed as a high throughput method with the focus on calculations with low computational cost yielding a relative change of the cell volume with and without spin polarization, rather than obtaining an accurate magnetic moment. The local structure observed using high-angle annular dark field imaging presented in Figure 1d agrees well with what is expected for the reported structure of MnZnSb[22] but the electron diffraction (ED) data suggests a small distortion of the cell from a tetragonal to a closely related triclinic cell. HAADF imaging also suggests the presence of strain in the material (Figure S3, Supporting Information). These observations motivated the collection of high-resolution
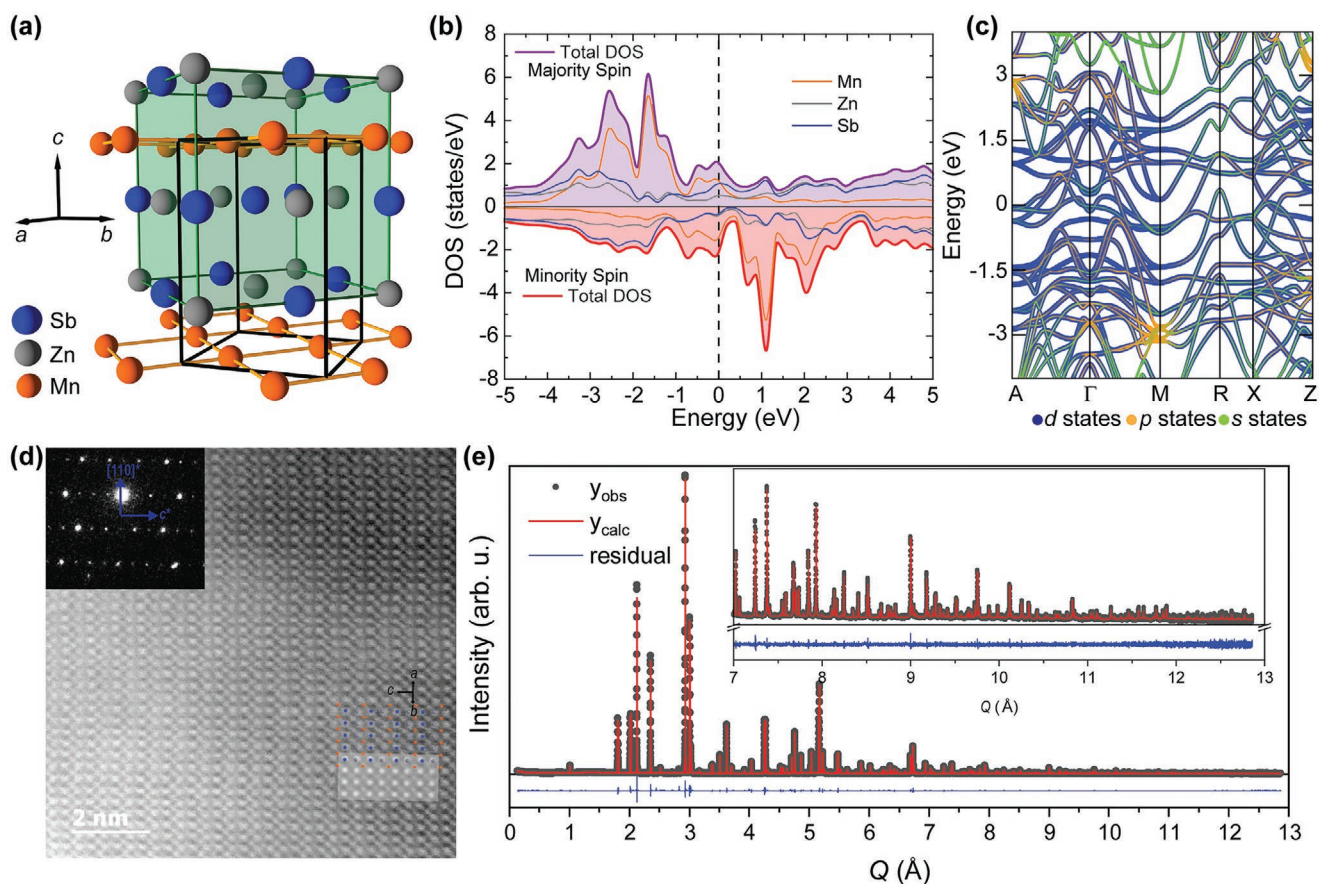
Figure 1. a) Prototypical structural model of the PbFCl structure for MnZnSb. The tetragonal unit cell is represented with the black cuboid. The structure is described by square net layers of Mn atoms (orange spheres) intercalated in a NaCl like blocks (green shaded cube) composed of Zn (grey spheres) and Sb (blue spheres) atoms. b) Total (purple-majority and red-minority spins) and atomic contributions (Mn-orange line, Zn-grey line, and Sb-blue line) spin-polarized density of states. c) Fat band electronic band structure along selected high symmetry directions with Mn d (blue), p (orange) and s (green) orbital projection for MnZnSb. Orbital character is used to distinguish between the flat bands (d states) and hybridized itinerant, broad bands (s-p states) about the Fermi level. d) [110] oriented HAADF image of a single MnZnSb grain with corresponding calculation and atomic projection (bottom right inset). The top left inset shows a corresponding electron diffraction pattern. e) Le Bail fitting (red line) of synchrotron X-ray diffraction data (black dots) using a triclinic MnZnSb cell with anisotropic strain broadening. The blue line represents the residual of the fit. The high Q region is shown in the inset.

synchrotron X-ray diffraction (SXRD) data. Initial Le Bail profile fits of the SXRD data using the reported tetragonal cell yielded a R_{wp} (a measure of the error in a Le Bail fit) of 11.54% with clear residual under certain Bragg peaks such as the (112) reflection (Figure S4, Supporting Information) confirming the need to lower the symmetry of the cell as suggested by the ED data. Le Bail profile fits using a triclinic cell resolved some of the peak shape issues observed previously by splitting them by small amounts in Q and resulted in a lower $R_{wp} = 10.72\%$ (Figure S5, Supporting Information) but highlighted some peak shape discrepancies which required the use of an anisotropic peak broadening model.[27] The final Le Bail fit is presented in Figure 1e with a $R_{wp} = 9.09\%$ and cell dimensions $a = 4.176\,89(5)$ Å, $b = 4.175\,73(2)$ Å, $c = 6.223\,73(4)$ Å, $\alpha = 89.9864(9)°$, $\beta = 90.020(1)°$ and $\gamma = 90.0157(7)°$. It is worth noting that the peak broadening observed is solely attributed to microstrain in the sample.

The MCE for the synthesized MnZnSb polycrystals is quantified through the extraction of the magnetic entropy change. The magnetic entropy change was calculated by the integration of isothermal magnetizations between 260–330 K and 0–7 T

(Figure S6, Supporting Information) using standard methodology outlined in the Supporting Information[28] and is shown in **Figure 2**a, exhibiting a maximum $\Delta S_{M(2T)} = 1.8$ J kg^{-1} K^{-1} at 311 K. This is an atypically significant $\Delta S_{M(2T)}$ considering the small magnetic moment observed in this compound (1.6(2) μ_B/f.u.) and is comparable to other compounds with $\Sigma_M \approx 2\%$ which present much larger magnetic moments (Y_2Fe_{17}, $\Delta S_{M(2T)} = 2.5$ J kg^{-1} K^{-1}, 2.2 μ_B/Fe, $T_C = 300$ K[29]). This magnitude of magnetic entropy change is further evidence of the validity of magnetic deformation as a computational proxy for magneto-caloric identification, through application upon a previously untested family of compounds. The isobaric heat capacity C_p shows the typical λ anomaly with an excess heat capacity around T_C with a value of 425 J K^{-1} kg^{-1} (Figure S7, Supporting Information) resulting in an adiabatic temperature change $\Delta T_{ad(2T)} = -T\Delta S_{M(2T)}/C_p = 1.15(5)$ K which is consistent with direct measurements performed on MnZnSb[21] and comparable to the most relevant conventional SOPT and inverse FOPT materials.[9] To understand the origin of the large MCE observed in MnZnSb it is important to have a clear picture of
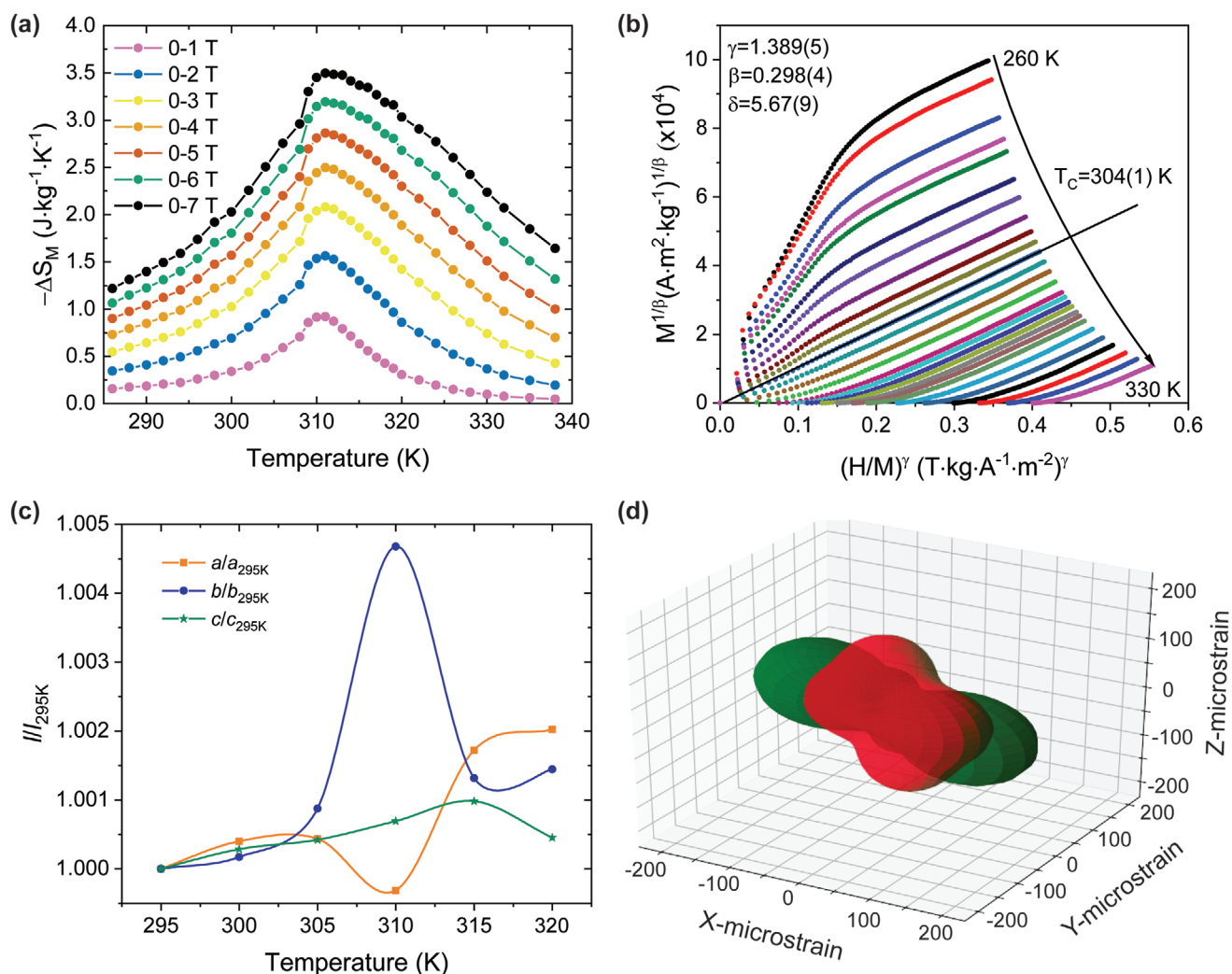
Figure 2. a) Magnetic entropy change (ΔS_M) for MnZnSb between 285 and 340 K in magnetic field changes from 1 to 7 T with a magnetic field independent ΔS_M maximum observed at 310 K. b) Arrott–Noakes plot for the isothermal magnetization of MnZnSb measured between 260 and 330 K. The extracted critical exponents are $\gamma = 1.389(5)$ and $\beta = 0.298(4)$ with a $T_C = 304$ K (black straight line). c) Relative change of MnZnSb lattice parameters (a-orange square, b-blue dots, and c-green stars. Lines are guides to the eyes) with respect to their 295 K value obtained from Le Bail fittings of temperature dependent PND using a triclinic cell. d) 3D representation of the strain tensor obtained from SXRD Le Bail fittings including anisotropic broadening below the T_C of MnZnSb (green) and above the T_C of $Mn_{0.9}Fe_{0.1}ZnSb$ (red).

the dimensionality, critical behavior, and possible magneto-structural anomalies as critical fluctuations around transitions are the underlying mechanism in controlling magnetic entropy. Through the construction of a standard Arrott plot[30] with mean-field critical exponents (Figure S8, Supporting Information) it is clear that MnZnSb is not described by mean-field theory as the isotherms are not parallel at high field. The Arrott plot presents positive slopes which is indicative of a SOPT as per the Banerjee criterion.[31] In order to obtain the precise critical exponents, an iterative method has been used (Supporting Information) resulting in the Arrott–Noakes plot[32] shown in Figure 2b with the extracted exponents in good agreements with the theoretical values for the 2D long-range mechanism[33] (Table S2, Supporting Information) and a $T_C = 304(1)$ K. The isothermal magnetizations all fall into two independent branches when using the scaling equation of state

(Figure S9, Supporting Information) and the exponents extracted from the power laws of field dependent magnetization and magneto-caloric properties (Figure S10, Supporting Information) confirm the reliability of the obtained exponents and indicates that the system belongs to a unique universality class in contradiction to a previous report where a 2D character in the zero-field susceptibility was observed while exhibiting a 3D character in the isothermal magnetization.[34] Considering that the dimensionality of the magnetism is confirmed to be 2D, the large magneto-caloric properties observed in MnZnSb could originate from anisotropic magneto-elastic coupling driven by the competition between the Mn moment ordering and structural distortion as recently observed in MnB.[18] The temperature dependent powder neutron diffraction (PND) collected around the T_C were refined using the triclinic model described earlier to extract the lattice parameters and the rela-

tive change of lattice parameters $l/l_{295\,K}$ between 295 and 320 K are shown in Figure 2c with a large positive and negative coefficient of thermal expansion anomaly around the T_C in the a and b directions respectively whereas the c lattice parameter is relatively invariant with respect to temperature. This variation of lattice parameter in the square net plane translates to a cell volume change of 0.18% (Figure S11, Supporting Information) which is similar to what is observed in the itinerant metamagnetic Laves phase $DyCo_2$ with a calculated structural entropy change of 4 J K^{-1} kg^{-1}[35] suggesting that the large MCE observed is driven by the strong magnetoelastic coupling between the crystallographic strain release and the formation of magnetic moment on the Mn square net. It is further supported by the observation of significant peak shape change through the T_C in the PND data (Figure S12, Supporting Information) and the observed change in the anisotropic strain obtained from SXRD for MnZnSb ($T_C = 304(1)$ K) and $Mn_{0.9}Fe_{0.1}ZnSb$ ($T_C = 279(1)$ K) measured below and above their respective T_C (Figure 2d). The remarkable decrease of T_C by substituting Mn with Fe is similar to what has been reported in the MnAlGe system where a weak correlation between T_C and the average number of d electrons per transition-metal atoms was proposed.[20] The possibility to finely tune T_C using chemical composition is an asset in designing magnetocaloric materials[10,36–40] and developing a predictive model of a descriptor controlling this effect would help guide the synthesis of new compounds. Comprehensive structural[41] and electronic[42] sorting maps in the PbFCl and related families have been built identifying the quantity c/a as a useful descriptor. However, predicting the c/a ratio of structures from a wide variety of bonding characters (e.g., ionic, covalent, metallic) can be difficult, and standard models are often limited to a specific structure-type and often fail without prior knowledge of the adequate descriptor to use.[43] Owing to the importance of the c/a parameter,[43] random forests were used to predict c/a using the experimental data available in the ICSD[44] as well as a hand curated dataset of 65 PbFCl type structures obtained from Pearson's database.[45] Random forests are a supervised machine learning method popular due to their ease of use and effectiveness with little to no hyperparameter tuning. They return the modal or mean prediction (for classification or regression tasks respectively) found by their constituent decision trees, which are trained on random subsets (bags) of data, splitting bags recursively to minimize entropy at each branch of the tree based on a random subset of data features. Predicting c/a of a material from the compound's formulae was found to be effective using this machine learning algorithm (the best r^2 was 0.78 on PbFCl data, Figure S13, Supporting Information; or 0.69 on ICSD data). This demonstrates the ability of random forests to work effectively on small datasets, where no larger datasets are available. However, most functional properties are tuned through substitution studies, where the researcher wishes to alter a known (parent) compound to find a better performing child compound. A more effective application of random forests was developed to predict c/a of an arbitrary child composition relative to the c/a of a known parent structure. Although the contributing factors that determine c/a cannot be easily enumerated, they are present to such an extent in the training data that machine learning methods can be used to approximate them in both models. The most effective model

to predict the change in c/a ratio between parent and child compound was trained using 80 000 randomly picked parent-child pairs of compounds in the ICSD, with the random forest being given as input the compositions of both parent and child structures as well as lattice parameters for the parent compound. When evaluating such a model, one could examine relations between predicted child c/a $(c_2/a_2)_{pred}$ and the true child c/a $(c_2/a_2)_{true}$; this leads to $r^2 = 0.95$. Alternatively, one could look at the success of the model in making predictions for the child c/a (c_2/a_2) in comparison to the parent compound (c_1/a_1), which we call r^2_{comp}; this leads to $r^2_{comp} = 0.97$ (**Figure 3**a). This model correctly predicted the direction of change in c/a 97% of the time, and is referred to as the accuracy, or ordinal accuracy. We also report the mean error of our model's c/a relative to the size of the c/a being predicted (MRE); here, MRE = 0.03. Using just the PbFCl structure type and related families to train such a model (a training set size of only 878), resulted in $r^2 = 0.87$ and an accuracy of 0.95. While substantial datasets such as the ICSD improve performance if they are available, good application of machine learning methods can obtain comparable results on smaller, more specialized, datasets where chemistries and/or structures are more similar. The accuracy of the prediction of the direction of change in a substituted compound was found to improve with the size of the change in c/a (Figure S14, Supporting Information). For very small changes, the model ordinal accuracy is better than a guess (and also better than trying to use a naive model using the weighted average of Shannon Ionic radii, Figure S15, Supporting Information), and this improves with larger changes in c/a. However, r^2 of the model shows no correlation for small changes, but improves dramatically after the difference in c/a values is greater than 7% (Figure S14, Supporting Information). While this ordinal accuracy is always better than a guess, for small changes in c/a, the accuracy is not sufficient to be assured of correct predictions, particularly where small numbers of chemical reactions are involved such as in this case. This could be partially attributed to dataset noise, with members of the ICSD being synthesized and measured using different protocols and instruments, where changes of less than 1% of c/a could be attributed to instrument error, making these data of insufficient precision for the required predictions. Nevertheless, we show random forests produced here are viable tools to guide synthetic experiments and demonstrate reasonable performance, producing a c/a ratio when given an arbitrary composition without the need for researchers to enumerate contributing factors. In practice, an investigator will have a parent compound in mind and is looking for chemical substitution to produce a child compound. Accordingly, we developed a tool with input data well matched to these circumstances (taking parent and child compositions and parental lattice parameters), this model also performs the best of all models tested.

The tunability of the T_C in the MnZnSb compound and its strong correlation with c/a is clearly demonstrated with the substitution of Mn with Fe and Cr (Figure 3b) with each T_C extracted from Arrott–Noakes plots (Figure S16, Supporting Information). This correlation is not localized around the MnZnSb compound but is observed across the other known ferromagnetic compounds MnAlGe and MnGaGe (Figure 3b), highlighting the partially ionic character of the magnetic
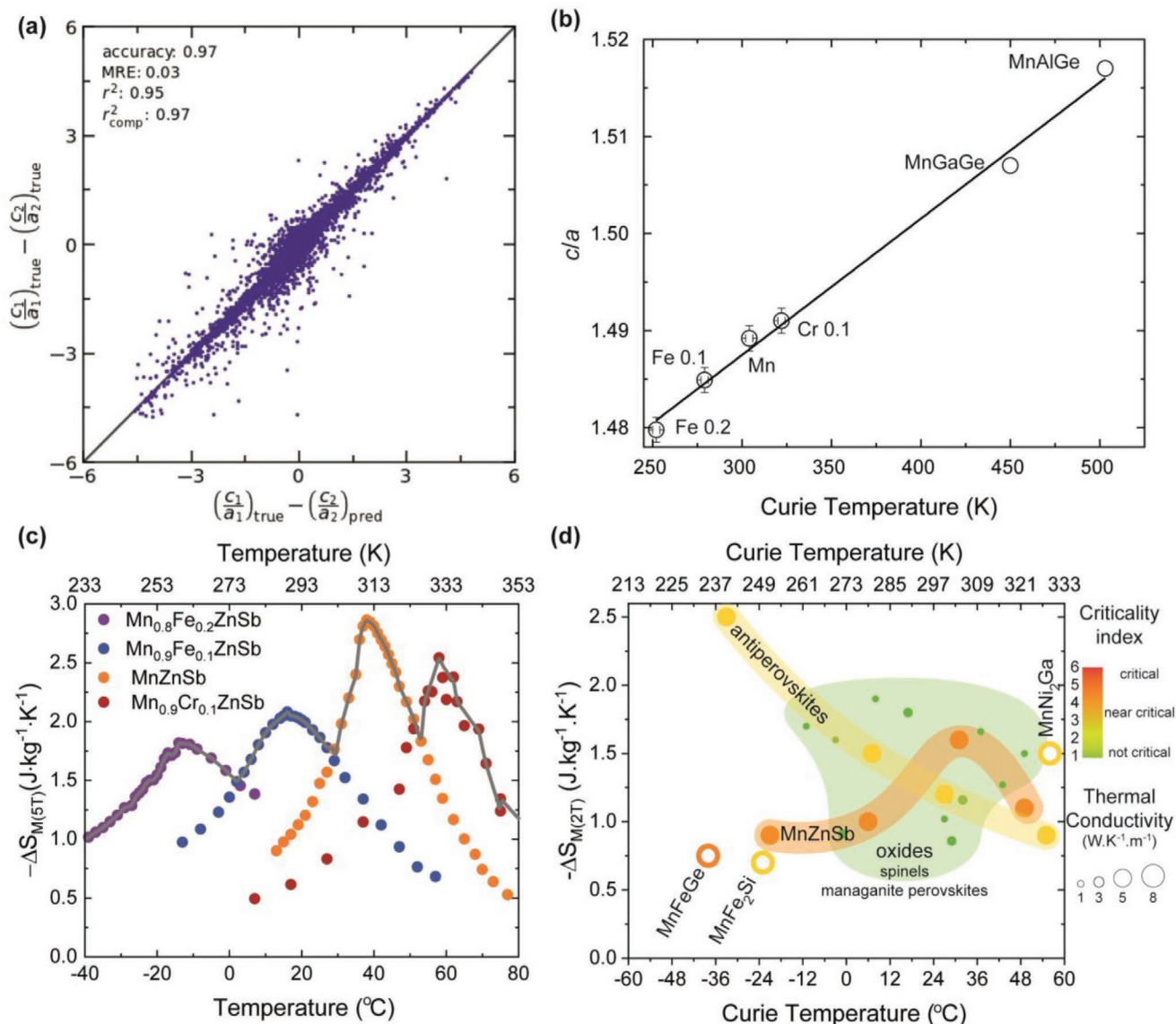
Figure 3. a) Comparison between the machine learning model predicted c/a for a child composition and the c/a of the parent composition. r^2 is relationship between the predicted c/a of the child composition and the true c/a. r^2_{comp} examines the ability of the model to predict the comparison between the child and parent composition as depicted. b) Variation of the c/a for the chemically substituted MnZnSb as a function of T_C extracted from Arrott–Noakes plots together with the literature reported values for MnAlGe[60] and MnGaGe.[61] The black line is a linear fit to the data highlighting the correlation over the whole range of compounds. c) Magnetic entropy changes between 0 and 5 T as function of temperature for $Mn_{0.9}Cr_{0.1}ZnSb$ (red dots), MnZnSb (orange dots), $Mn_{0.9}Fe_{0.1}ZnSb$ (blue dots), and $Mn_{0.8}Fe_{0.2}ZnSb$ (purple dots) The grey line outlines the combined isothermal for the four different compositions. d) Isothermal entropy changes for selected magneto-caloric materials in a magnetic field of 2 T as a function of their Curie temperature. Empty and full symbols correspond to FOPT and SOFPT materials respectively. The criticality and the thermal conductivity of the considered compounds are represented by the color and the size of the data points respectively. Every data point stands for a single sample. The data and references used to construct this diagram can be found in Table S3, Supporting Information.

interaction in these compounds with the exchange susceptible to small change in the interatomic distances. The associated reduction in the saturation magnetization in the substituted compounds (Figure S17, Supporting Information) follows the trend observed and rationalized for MnGaGe[46] and leads to a reduction in the maximum MCE (Figure 3c). The observation that the saturation magnetization of $Mn_{0.8}Fe_{0.2}ZnSb$ is 21% that of MnZnSb whilst the magnetic entropy change remains 65% confirms that the coupling between magnetic moment formation on the square net and the change of cell volume around

the Curie temperature is the major contributor to the total entropy change through the ferromagnetic transition. The values for $\Delta S_{M(2T)}$ for the tuned alloys can be found in Table S3, Supporting Information. In the context of near room temperature SOPT magnetocaloric materials, the performance of these alloys is summarized in Figure 3d, and is found to outperforms the non-critical compounds in the secondary application parameters (Table S3, Supporting Information) with a higher density (7 g cm^{-3}), a thermal conductivity $\kappa = 4$ W K^{-1} m^{-1} at 300 K (Figure S18, Supporting Information) close to the

threshold value of 5 W K^{-1} m^{-1} for optimum cooling power in a regenerator,[47] and a relatively low heat capacity.

3. Conclusions

This study gives a new insight on the magnetic transition in the ferromagnetic compound MnZnSb and the origin of the MCE in this system through the combination of theoretical and experimental approaches. An array of structural characterization techniques were used to evaluate the relationship between crystallographic strain and magnetic ordering within this system and its influence upon the entropy change through the ferromagnetic transition. Furthermore, the detailed critical exponent analysis of this compound has enabled the system to be ascribed to one universality class across all order parameters and identified as "2D long-range." Despite the small magnetic moments measured in these systems, the moderate MCE observed is attributed to the release of crystallographic strain through the magnetic transition. A strong correlation between magnetic ordering temperature and the crystallographic parameter c/a was found and used to tune the temperature range of MnZnSb over a 90 K span around room temperature. We expanded upon the realization of the intimate relationship between the crystallographic parameter c/a and transition temperature within this family to construct a machine learning algorithm to develop a predictive c/a model that can be used for future exploratory synthesis.

4. Experimental Section

Computational Methods: First principles calculations were carried out with the Vienna ab initio simulation package (VASP).[48,49] These calculations in VASP were performed using the projector augmented wave pseudopotentials within the PBE-GGA framework.[50,51] The structures were relaxed with and without spin-polarization, corresponding to a collinear ferromagnetic ground state and a non-magnetic ground state, respectively. Relaxation was performed on 8 × 8 × 8 Monkhorst–Pack (MP) k-mesh. The total energy was found to be converged to within 1 × 10^{-8} eV atom^{-1} using a plane wave cutoff of 500 eV. Geometry optimizations were considered to be converged when the forces on each atom were reduced to less than 0.001 eV Å^{-1}. DOS calculations were performed with a 24 × 24 × 24 MP k-mesh. Further calculations were performed using experimental lattice parameters, PBEsol functional plus Hubbard corrections,[52] and disordered systems. All results are available in Table S1, Supporting Information. Magnetic deformations were calculated following the method described by Bocarsly et al.[17] and band structure plots were generated using the SUMO package.[53] Details of the methods can be found in the Supporting Information.

Machine Learning Algorithms: Sci-kit learn's implementation of Random Forrest Regressors were used with default hyperparameters (as of version 0.22) for all experiments. All metrics quoted in the main section of this paper are based on an 80–20 training test split, with "leave one cluster out cross validation"[54] scores for these metrics also available in the Supporting Information. ICSD data used was complete as of 2017 and the materials project's tetragonal structures were complete as of 2019. A detailed discussion of the methods can be found in the Supporting Information. All codes needed to recreate these experiments are available on github (https://github.com/lrcfmd/RandomForestsForPredictingUnitCellProperties).

Synthesis of the Materials: Stoichiometric proportions of the required elements (manganese Alfa Aesar 99.95%, zinc Sigma Aldrich 99.995%, antimony Alfa Aesar 99.999%, iron Alfa Aesar 99.998%, and chromium Sigma Aldrich >99%) were dry-mixed using a pestle and mortar,

sealed in evacuated quartz tubes in less than 10^{-4} Torr, and placed in a muffle furnace at 1273 K for 6 h with hourly agitation. The samples were quenched in ice water from 1273 K, reground and resealed under the same evacuation conditions, and annealed at 773 K for 10 days followed by quench cooling. Four samples were produced MnZnSb, Mn$_{0.9}$Cr$_{0.1}$ZnSb, Mn$_{0.9}$Fe$_{0.1}$ZnSb, and Mn$_{0.8}$Fe$_{0.2}$ZnSb.

Structural Characterization: Phase identification was performed on all the samples using X-ray diffraction on a Rigaku Smartlab diffractometer with monochromatic Cu K$_\alpha$ radiation. Temperature dependent powder neutron diffraction was carried out on MnZnSb powder using the D20 diffractometer at the Institut Laue-Langevin.[55] To collect data across the magnetic transition, D20 was operated in the intermediate-resolution mode using the wavelength of 1.54 Å as provided by the Ge monochromator take-off angle of 90°. This setting ensured a relatively high neutron flux on the sample ($\approx$1.5 × 10^7 n cm^2 s^{-1}) and resolution approaching $\Delta d/d \approx 2.9 \times 10^{-3}$, which is good enough for most structural studies. $\approx$4 g of MnZnSb powder were contained in a thin-walled vanadium cylindrical can of 7 mm diameter, which was placed in a standard orange cryofurnace. Isothermal datasets were acquired for 60 min every 5 K in the temperature range 290–320 K. SXRD was performed on MnZnSb, Mn$_{0.9}$Cr$_{0.1}$ZnSb, and Mn$_{0.9}$Fe$_{0.1}$ZnSb using the 11-BM diffractometer at the Advanced Photon Source (Argonne National Laboratory) with a wavelength of 0.4128 37 Å. Le Bail fittings were carried out using FullProf[56] and JANA2006[57] freeware. The profile parameters used during Le Bail fitting are from provided standards data of SRM 660a (LaB$_6$) and NACALF for the 11-BM and D20 data respectively.

The powder MnZnSb sample was analyzed by various transmission and scanning electron microscopy techniques such as diffraction and atomic imaging techniques. This work was carried out with a JEOL 2010 microscope equipped with a precession module (DIGISTAR system) and a JEOL ARM200 double corrected (Imaging and probe) microscope. Both microscopes are equipped with EDX analyzers, INCA-oxford and CENTURION–JEOL spectrometers, respectively. A part of the sample was crushed into a mortar with alcohol and a few droplets were deposited onto a copper grid. To avoid carbon contamination during the observations and collections of chemical mapping, the grid was first treated with an ion cleaner for 5 min before loading in the microscope. The ED data have been collected with a precession angle of 1.2° in the tilting range of −50° to 50° by 1° tilt step. All these precession electron diffraction tomography data have been compiled and rescaled owing to PETS software[58] in a single data set. The cell and structural determinations have been obtained with the JANA2006 software[57] while the simulated ADF images have been calculated with the JEMS software[59] considering the convolution of the STEM probe with the intensity of the object (square of the projected potential multiplied by the electron-matter interaction constant of the structure).

Physical Characterization: Magnetic measurements were performed on a Quantum Design MPMS vibrating sample magnetometer. Isothermal magnetization as a function of magnetic field between 0 and 7 T was measured with 1 K intervals in the region about the T_C as estimated from the first derivative of temperature dependent magnetization measurements. These isotherms were used both in critical exponent analysis and the magnetocaloric study. Heat capacity and thermal conductivity were measured using a Quantum Design Dynacool and PPMS respectively. The thermal conductivity was measured using the Thermal Transport Option in a bar geometry cut from an ingot of MnZnSb.

Supporting Information

Supporting Information is available from the Wiley Online Library or from the author.

Acknowledgements

Conflict of Interest

The authors declare no conflict of interest.

Data Availability Statement

The data that support the findings of this study are openly available in The University of Liverpool Data Catalogue at http://datacat.liverpool.ac.uk/id/eprint/120.

Keywords

[1] G. V. Brown, *J. Appl. Phys.* **1976**, *47*, 3673.
[2] V. Franco, J. S. Blázquez, B. Ingale, A. Conde, *Annu. Rev. Mater. Res.* **2012**, *42*, 305.
[3] W. F. Giauque, D. P. MacDougall, *Phys. Rev.* **1933**, *43*, 768.
[4] S. Y. Dan'kov, A. M. Tishin, V. K. Pecharsky, K. A. Gschneidner, *Phys. Rev. B* **1998**, *57*, 3478.
[5] V. K. Pecharsky, J. K. A. Gschneidner, *Phys. Rev. Lett.* **1997**, *78*, 4494.
[6] V. A. Chernenko, J. M. Barandiarán, J. R. Fernández, D. P. Rojas, J. Gutiérrez, P. Lázpita, I. Orue, *J. Magn. Magn. Mater.* **2012**, *324*, 3519.
[7] T. Kato, K. Nagai, T. Aisaka, *J. Phys. C: Solid State Phys.* **1983**, *16*, 3183.
[8] N. H. Dung, L. Zhang, Z. Q. Ou, E. Brück, *Scr. Mater.* **2012**, *67*, 975.
[9] T. Gottschall, K. P. Skokov, M. Fries, A. Taubel, I. Radulov, F. Scheibel, D. Benke, S. Riegg, O. Gutfleisch, *Adv. Energy Mater.* **2019**, *9*, 901322.
[10] J. A. Turcaud, Ph.D. Magnetocaloric effect and thermal transport management in lanthanum manganites, Imperial College, London **2014**.
[11] A. Rostamnejadi, M. Venkatesan, J. Alaria, M. Boese, P. Kameli, H. Salamati, J. M. D. Coey, *J. Appl. Phys.* **2011**, *110*, 043905.
[12] S. Singh, L. Caron, S. W. DSouza, T. Fichtner, G. Porcari, S. Fabbrici, C. Shekhar, S. Chadov, M. Solzi, C. Felser, *Adv. Mater.* **2016**, *28*, 3321.
[13] C. P. Bean, D. S. Rodbell, *Phys. Rev.* **1962**, *126*, 104.
[14] B. P. Alho, N. A. Oliveira, V. S. R. Sousa, E. J. R. Plaza, A. M. G. Carvalho, P. J. Ranke, *J. Phys.: Condens. Matter* **2010**, *22*, 486008.
[15] M. W. Gaultois, T. D. Sparks, C. K. H. Borg, R. Seshadri, W. D. Bonificio, D. R. Clarke, *Chem. Mater.* **2013**, *25*, 2911.
[16] D. H. Fabini, M. Koerner, R. Seshadri, *Chem. Mater.* **2019**, *31*, 1561.
[17] J. D. Bocarsly, E. E. Levin, C. A. C. Garcia, K. Schwennicke, S. D. Wilson, R. Seshadri, *Chem. Mater.* **2017**, *29*, 1613.
[18] J. D. Bocarsly, E. E. Levin, S. A. Humphrey, T. Faske, W. Donner, S. D. Wilson, R. Seshadri, *Chem. Mater.* **2019**, *31*, 4873.
[19] N. Y. Pankratov, V. I. Mitsiuk, V. M. Ryzhkovskii, S. A. Nikitin, *J. Magn. Magn. Mater.* **2019**, *470*, 46.
[20] T. Kanomata, H. Endo, S.-i. Mori, S. Sakatsume, H. Yoshida, T. Kaneko, *Jpn. J. Appl. Phys.* **1993**, *32*, 269.
[21] T. Kamimura, H. Ido, K. Shirakawa, *J. Appl. Phys.* **1985**, *57*, 3255.
[22] V. Johnson, W. Jeitschko, *J. Solid State Chem.* **1977**, *22*, 71.
[23] V. Singh, S. Karmakar, R. Rawat, P. Kushwaha, *J. Appl. Phys.* **2019**, *125*, 233906.
[24] T. Kanomata, H. Endo, S. Mori, H. Okajima, T. Hihara, K. Sumiyama, T. Kaneko, K. Suzuki, *J. Magn. Magn. Mater.* **1995**, *143*, 133.
[25] A. Kimura, S. Suga, H. Matsubara, T. Matsushita, Y. Saitoh, H. Daimon, T. Kaneko, T. Kanomata, *Solid State Commun.* **1992**, *81*, 707.
[26] V. P. Dymont, G. I. Makovetskii, V. M. Ryzhkovskii, *Phys. Status Solidi A* **1988**, *107*, K89.
[27] P. W. Stephens, *J. Appl. Cryst.* **1999**, *32*, 281.
[28] A. M. Tishin, Y. I. Spichkin, *The Magnetocaloric Effect and its Applications*, Taylor & Francis, London **2003**.
[29] J. L. S. Llamazares, P. Álvarez-Alonso, C. F. Sánchez-Valdés, P. J. Ibarra-Gaytán, J. A. Blanco, P. Gorria, *Curr. Appl. Phys.* **2016**, *16*, 963.
[30] A. Arrott, *Phys. Rev.* **1957**, *108*, 1394.
[31] B. K. Banerjee, *Phys. Lett.* **1964**, *12*, 16.
[32] A. Arrott, J. E. Noakes, *Phys. Rev. Lett.* **1967**, *19*, 786.
[33] M. E. Fisher, S. K. Ma, B. G. Nickel, *Phys. Rev. Lett* **1972**, *29*, 917.
[34] F. Ono, X. Hu, N. Fujii, K. Hayashi, N. Okada, S. Endo, T. Kanomata, *Phys. B* **1997**, *237*, 162.
[35] K. A. Gschneidner, Y. Mudryk, V. K. Pecharsky, *Scr. Mater.* **2012**, *67*, 572.
[36] K. P. Skokov, K.-H. Müller, J. D. Moore, J. Liu, A. Y. Karpenkov, M. Krautz, O. Gutfleisch, *J. Alloys Compd.* **2013**, *552*, 310.
[37] K. P. Skokov, A. Y. Karpenkov, D. Y. Karpenkov, O. Gutfleisch, *J. Appl. Phys.* **2013**, *113*, 17A945.
[38] F. Guillou, H. Yibole, G. Porcari, L. Zhang, N. H. Dijk, E. Brück, *J. Appl. Phys.* **2014**, *116*, 063903.
[39] T. Gottschall, K. P. Skokov, R. Burriel, O. Gutfleisch, *Acta Mater.* **2016**, *107*, 1.
[40] K. Katagiri, K. Nakamura, H. Wada, *J. Alloys Compd.* **2013**, *553*, 286.
[41] J. Nuss, U. Wedig, M. Jansen, *Z. Kristallogr.- Cryst. Mater.* **2006**, *221*, 554.
[42] S. Klemenz, S. Lei, L. M. Schoop, *Annu. Rev. Mater. Res.* **2019**, *49*, 185.
[43] M. G. Brik, A. Suchocki, A. Kamińska, *Inorg. Chem.* **2014**, *53*, 5088.
[44] M. Hellenbrandt, *Crystallogr. Rev.* **2004**, *10*, 17.
[45] K. C. P. Villars, *Pearson's Crystal Data: Crystal Structure Database for Inorganic Compounds*, ASM International, Almere **2019**.
[46] J. B. Goodenough, G. B. Street, K. Lee, J. C. Suits, *J. Phys. Chem. Solids* **1975**, *36*, 451.
[47] K. K. Nielsen, K. Engelbrecht, *J. Phys. D: Appl. Phys.* **2012**, *45*, 145001.
[48] G. Kresse, J. Furthmüller, *Phys. Rev. B* **1996**, *54*, 11169.
[49] G. Kresse, J. Hafner, *Phys. Rev. B* **1993**, *47*, 558.
[50] P. E. Blöchl, O. Jepsen, O. K. Andersen, *Phys. Rev. B* **1994**, *49*, 16223.
[51] J. P. Perdew, K. Burke, M. Ernzerhof, *Phys. Rev. Lett.* **1997**, *78*, 1396.
[52] J. P. Perdew, A. Ruzsinszky, G. I. Csonka, O. A. Vydrov, G. E. Scuseria, L. A. Constantin, X. Zhou, K. Burke, *Phys. Rev. Lett.* **2008**, *100*, 136406.
[53] A. M. Ganose, A. J. Jackson, D. O. Scanlon, *J. Open Source Software* **2018**, *3*, 717.

[54] B. Meredig, E. Antono, C. Church, M. Hutchinson, J. Ling, S. Paradiso, B. Blaiszik, I. Foster, B. Gibbons, J. Hattrick-Simpers, A. Mehta, L. Ward, *Mol. Syst. Des. Eng.* **2018**, *3*, 819.

[55] S. Savvin, J. Alaria, P. A. E. Murgatroyd, *Magnetic structure of MnZnSb*, Institut Laue-Langevin, Grenoble **2018**, https://doi.org/10.5291/ILL-DATA.INTER-414.

[56] J. Rodriguez-Carvajal, *Matter* **1993**, *192*, 55.

[57] V. Petříček, M. Dušek, L. Palatinus, *Z. Kristallogr.- Cryst. Mater.* **2014**, *229*, 345.

[58] L. Palatinus, P. Brázda, M. Jeľínek, J. Hrdá, G. Steciuk, M. Klementová, *Acta Crystallogr., Sect. B: Struct. Sci., Cryst. Eng. Mater.* **2019**, *B75*, 512.

[59] www.jems-swiss.ch/Home/jemsWebSite/jems.html (accessed: June 2020).

[60] K. Adachi, S. Ogawa, *Pnictides and Chalcogenides I*, Springer-Verlag, Berlin **1988**.

[61] N. S. S. Murthy, R. J. Begum, C. S. Somanathan, M. R. L. N. Murthy, *J. Appl. Phys.* **1969**, *40*, 1870.